Evidence of large spin-orbit coupling effects in quasi-free-standing graphene on Pb/Ir(111)

M. M. Otrokov,[1,2] I. I. Klimovskikh,[3] F. Calleja,[4] A.M. Shikin,[3] O. Vilkov,[3] A.G. Rybkin,[3]
D. Estyunin,[3] S. Muff,[5,6] J.H. Dil,[5,6] A. L. Vázquez de Parga,[4,7] R. Miranda,[4,7]
H. Ochoa,[8] F. Guinea,[4,9] J.I. Cerdá,[10] E. V. Chulkov,[1,11,12,3] and A. Arnau[1,11,12]

[1]*Centro de Física de Materiales (CFM-MPC), Centro Mixto CSIC-UPV/EHU,*
20018 Donostia-San Sebastián, Basque Country, Spain
[2]*Tomsk State University, 634050 Tomsk, Russia*
[3]*Saint Petersburg State University, 198504 Saint Petersburg, Russia*
[4]*Instituto Madrileño de Estudios Avanzados en Nanociencia, Cantoblanco 28049, Madrid, Spain*
[5]*Institute of Physics, Ecole Polytechnique Fédérale de Lausanne, CH-1015 Lausanne, Switzerland*
[6]*Swiss Light Source, Paul Scherrer Institut, CH-5232 Villigen, Switzerland*
[7]*Departamento de Física de la Materia Condensada and IFIMAC,*
Universidad Autónoma de Madrid, Cantoblanco 28049, Madrid, Spain
[8]*Department of Physics and Astronomy, University of California, Los Angeles, California 90095, USA*
[9]*Department of Physics and Astronomy, University of Manchester, Oxford Road, Manchester M13 9PL, UK*
[10]*Instituto de Ciencia de Materiales de Madrid, Consejo Superior*
de Investigaciones Científicas, Cantoblanco 28049, Madrid, Spain
[11]*Donostia International Physics Center (DIPC),*
20018 Donostia-San Sebastián, Basque Country, Spain
[12]*Departamento de Física de Materiales UPV/EHU,*
20080 Donostia-San Sebastián, Basque Country, Spain
(Dated: May 8, 2018)
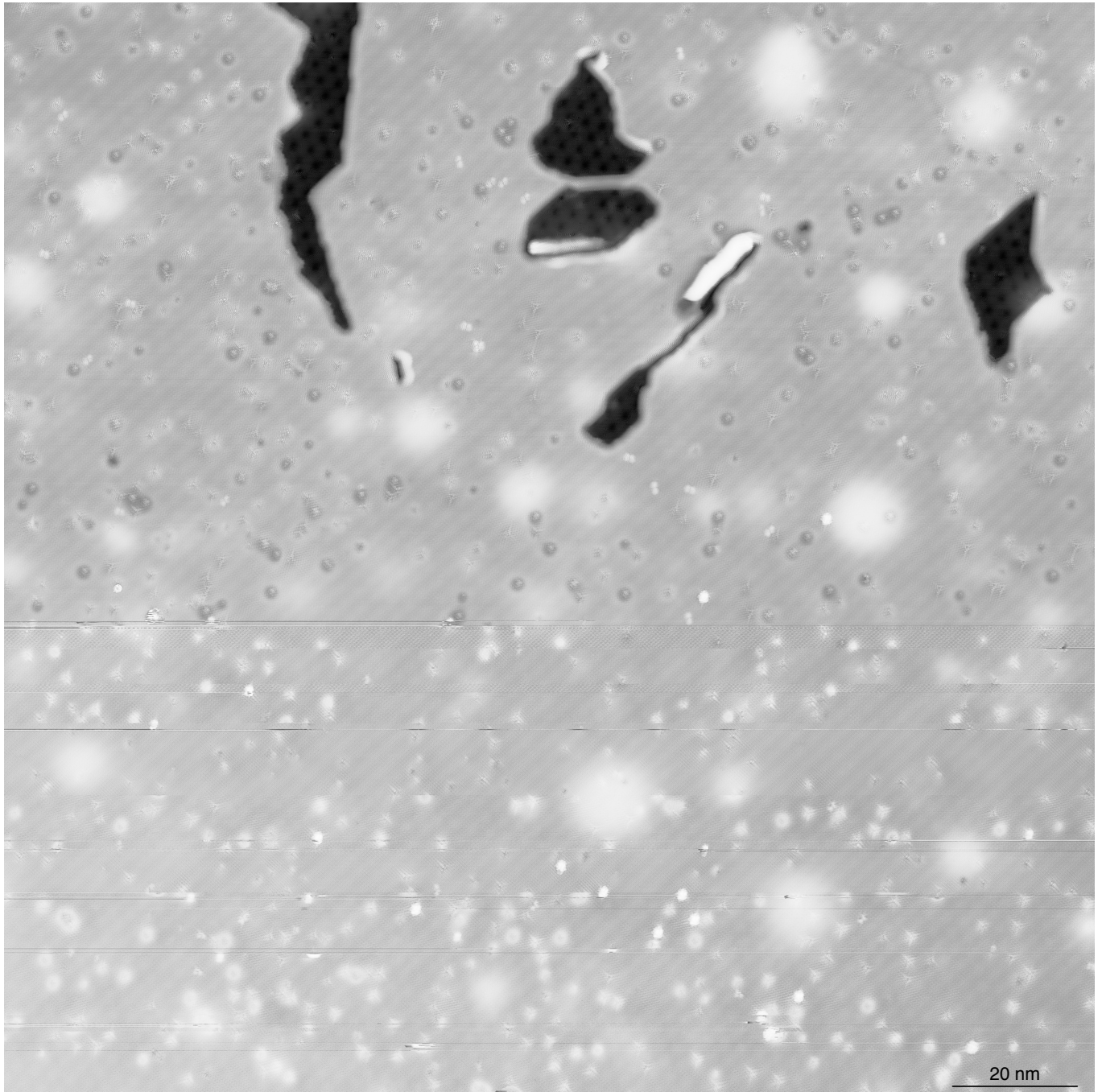
I. LARGE-SCALE STM IMAGE

Figure 1. STM topographic image corresponding to the FFT shown in Figure 1b of the main text. The whole area is contained in a single atomic terrace. The darker regions correspond to the non-intercalated gr/Ir parts, exhibiting the characteristic hexagonal moiré pattern. The brighter and more abundant region corresponds to gr/Pb/Ir(111), exhibiting a line-pattern produced by the lead structure. The intercalation ratio is above 90%. Imaging conditions: 3 mV bias and 300 pA tunneling current.
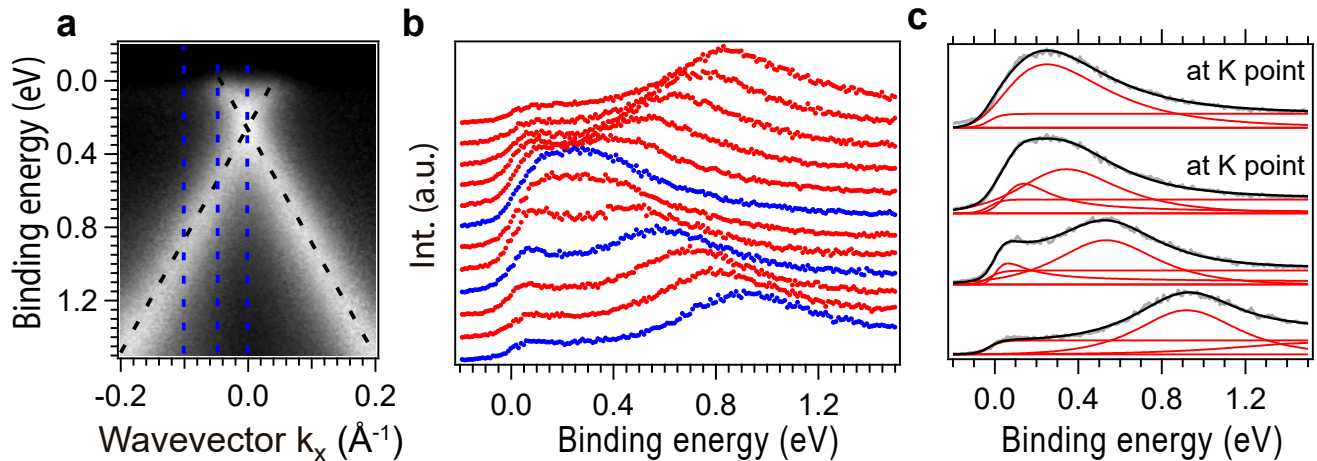
II. LINEWDITH ANALYSIS AT AND NEAR THE $\overline{K}$-POINT

Figure 2. (a) ARPES image of graphene/Pb/Ir(111) taken at a photon energy of 21.2 eV at the $\overline{K}$ point, along the direction, perpendicular to $\overline{\Gamma K}$. (b) EDC spectra obtained from the data shown in (a). (c) Decomposition results of EDC spectra, marked by blue lines in (a,b).

Fig. 2a shows the dispersion of graphene π-state, which is marked by the black dashed line. For the spectral decomposition, we have chosen three cuts which are marked with blue colour. The first from the bottom blue curve in Fig. 2b was cut at -0.1 Å^{-1}, the second at about -0.05Å^{-1} and the third in vicinity of the $\overline{K}$-point.

In Fig. 2c, the decomposition of the EDC spectra is presented. One can see that the first curve (from the bottom) can be fitted with a main peak centered at around 0.9 eV which we assign to graphene's π-state. In the second curve, the π-state moves towards the Fermi level (close to 0.55 eV), and the π^*-state appears very close to the Fermi level. The apparent width of the peak that corresponds to the π-state reaches the value FWHM = 560 meV (the Fermi level and background were chosen the same as for the previous spectrum). Finally, at the $\overline{K}$ point two cases of decomposition are presented (third and fourth spectra). They correspond to fitting with two peaks, related to π and π^*-states, or one single peak, respectively. Both of them fit the spectrum rather well and, again, do not permit to resolve finer spectral features. Taking into account the Fermi level vicinity and related asymmetric peak behavior one can estimate the apparent FWHM of the π-state at the $\overline{K}$ point to be ∼700 meV. Thus, the width of the graphene state increases at the $\overline{K}$ point by ∼140 meV, which is consistent with a spin-orbit splitting dominated by a Rashba term (assuming the absence of the Dirac point gap).
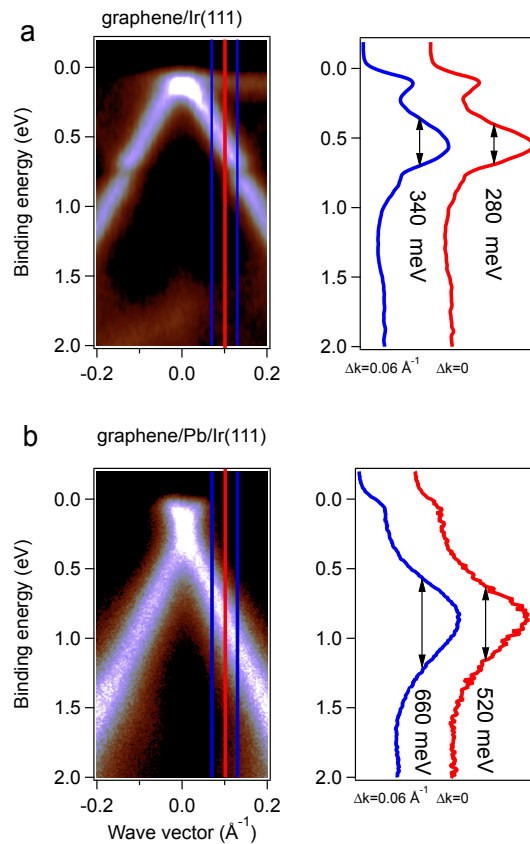
III.   LINEWDITH BROADENING AFTER THE PB INTERCALATION

Figure 3. ARPES images, taken at a photon energy of 21.2 eV near the $\overline{K}$ point of graphene along the direction perpendicular to $\overline{\Gamma K}$, for graphene/Ir(111) (a) and graphene/Pb/Ir(111) (b). The EDCs, taken at $k_{\parallel} = 0.1$ Å^{-1} with the angular acceptance of $\Delta k = 0.06$ Å^{-1} ($\Delta k = 0.0$ Å^{-1}) are presented in the right panels in blue (red).

In Fig. 3 we show the ARPES images acquired through the $\overline{K}$ point in the direction perpendicular to $\overline{\Gamma K}$, before (a) and after (b) the Pb intercalation under the same experimental conditions. In the right panels, the EDCs taken at $k_{\parallel} = 0.1$ Å^{-1} with an angular acceptance of $\Delta k = 0.06$ Å^{-1} are presented in blue (the same acceptance value as in the spin-resolved spectra presented in the main text). The EDCs acquired with the best resolution are shown in red. It is clearly seen that the apparent FWHM of the graphene peaks in the EDCs significantly increases after Pb atoms intercalation from 340 meV to 660 meV (for the particular value 0.06 Å^{-1} of the k acceptance). A comparison of the red curves yields a qualitatively similar result: 280 and 520 meV, respectively. Apart from the broadening produced by the increased k acceptance ($\Delta k = 0.06$ Å^{-1} both systems), the larger energy broadening in graphene/Pb/Ir(111) can be related to the presence of different rotational domains of Pb, imperfections of the intercalated layer, as well as to the hybridization with the blurred Pb/Ir(111) states. As explained in the manuscript and in the Supplementary Note VII, the projected gap of Ir(111) around the $\overline{K}$ point, where graphene π bands meet, is closed due to band folding in Pb/Ir(111). The consequence is an increase of the energy width of the corresponding Pb/Ir(111) surface resonances that, in turn, introduce an additional broadening in the π-bands, as observed in the ARPES data. Incidentally, the same effect is found in the calculated PDOS for graphene/Ir(111) shown in Figure 5a of the manuscript above the Fermi level (above the projected Ir(111) gap).

Now, the point is that such an enhancement in peak widths after Pb intercalation cannot be the result of a spin splitting enhancement only (from 50 meV in graphene/Ir to 100 meV in graphene/Pb/Ir) and, therefore, it does not allow us to compare the spin-resolved and spin-integrated spectra for the spin structure analysis. Note that similar FWHM enhancements have been observed in Ref. [1] after Bi atoms intercalation underneath graphene on Ir(111) and ascribed to the surface lattice disorder introduced by intercalation and to the hybridization with the underlying Bi atoms.
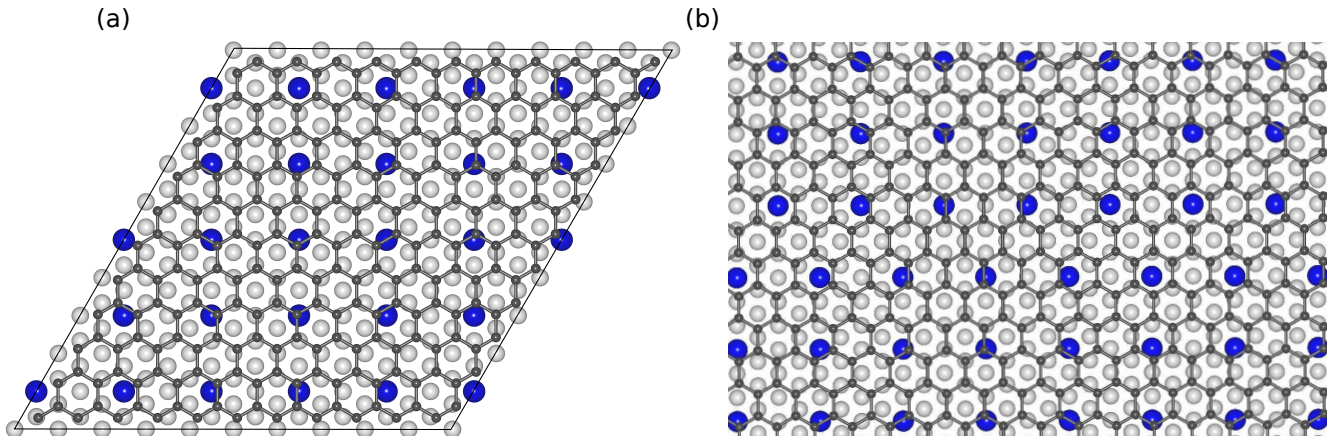
IV. VISUALIZATION OF UNIT CELLS

(a)

(b)

Figure 4. (a) gr/Pb/Ir(111) unit cell with the (10×10) periodicity. Blue, light grey and dark grey circles represent Pb, Ir and C atoms, respectively. This periodicity allows to model graphene with a lattice parameter $\sim$2.48 Å , which matches that of free-standing graphene ($\sim$2.46 Å) very well. However, one has to introduce a stacking fault in the Pb $c(4 \times 2)$ layer, as it is shown in (b). Note, that the stacking fault is not seen in (a). The presence of the stacking fault does not represent a problem since (i) Pb atoms do not come too close to each other, (ii) the Pb bands essentially disappear due to a strong hybridization with Ir(111), and (iii) the presence of such stacking faults in real samples is very likely.
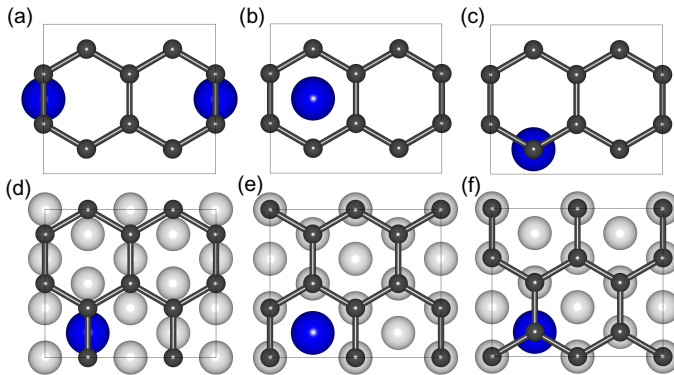

Figure 5. Unit cell with the $c(4 \times 2)$ periodicity used for modelling of gr*/Pb (a,b,c) and gr*/Pb/Ir(111) (d,e,f) with well-defined Pb registry with respect to graphene layer. Panels (a,d) correspond to the bridge, (b,e) – to the hollow, and (c,f) – to the top registry. Note that the graphene lattice parameter is stretched by $\sim$10% to form a commensurate structure. These two systems have to be considered as auxiliary systems that permit to explain qualitative trends observed in the real complete system, in which graphene is actually not commensurate with the Pb/Ir(111) substrate.

V.   THE EFFECT OF THE PB ROTATIONAL DOMAINS ON THE GRAPHENE SPIN TEXTURE.

Fig. 6 shows the spin textures of calculated graphene bands for the three rotational domains in the graphene/Pb/Ir(111) system. These data have been obtained using (8×8) supercells with three atomic layers of Ir, which is enough to understand the role played by the co-existence of different rotational domains in the observed spin texture. It is worth to mention at this point that, in Fig. 6, the domain 2 has the same orientation with respect to the graphene and Ir lattices as the one studied in the (10×10) cell (its structure in shown in the Supplementary Fig. 4 and the corresponding bandstructure – in Fig. 4 of the manuscript). In agreement with the result shown in Fig. 4 of the manuscript, there are no s_x spin components along k_x for the domain 2.

However, in the other two domains (i.e. domain 1 and domain 3, that can be obtained from the domain 2 by the rotation by -120° and +120°, respectively, see Fig. 7) the π-bands feature a finite value of the s_x spin components. These components are opposite and they have the same absolute value. Therefore, if these three Pb domains appear in the equal proportion at the Ir(111) surface, the total s_x averages to zero on the typically large scales of the ARPES spot size (100 microns for the synchrotron radiation). The typical size of the different Pb domains observed in STM images is below 100 nm, i. e., much smaller than the spot size. Based on this argument, we conclude that the s_x spin component is indeed expected to vanish along the k_x direction in our spin-ARPES experiments.

This is further supported by the following analysis based on the presence of time reversal symmetry $[s_x(k_x, k_y) = -s_x(-k_x, -k_y)]$ and the symmetry imposed by the existence of mirror planes like $x = 0$ in domain 2 $[s_x(k_x, k_y) = s_x(-k_x, k_y)]$, which implies $s_x(k_x, 0) = s_x(-k_x, 0)$ at $k_y = 0$ and, therefore, $s_x = 0$ for every $(k_x, 0)$ point (along the x axis). In domains 1 and 3, $x = 0$ is no longer a mirror plane $[s_x(k_x, 0) \neq 0]$ but the two domains are related by a mirror plane at $x = 0$ (Fig. 8) and, therefore, their spin components satisfy the relations:

$$s_x(k_x, 0, domain1) = -s_x(k_x, 0, domain3) \text{ and } s_{y/z}(k_x, 0, domain1) = s_{y/z}(k_x, 0, domain3).$$

So, if one sums the contributions from the domains 1 and 3, assuming equal weight for both, then the resulting spin component along the k_x vanishes:

$$s_x(k_x, 0, domain1 + domain3) = 0.$$

We can support the suggestion about the presence of the three Pb domains in (approximately) equal proportion based on LEED and STM data: 1) the LEED spots for the three domains appear to be equally intense and 2) the FFT STM images at the large scale also show equal intensity for the three domains.
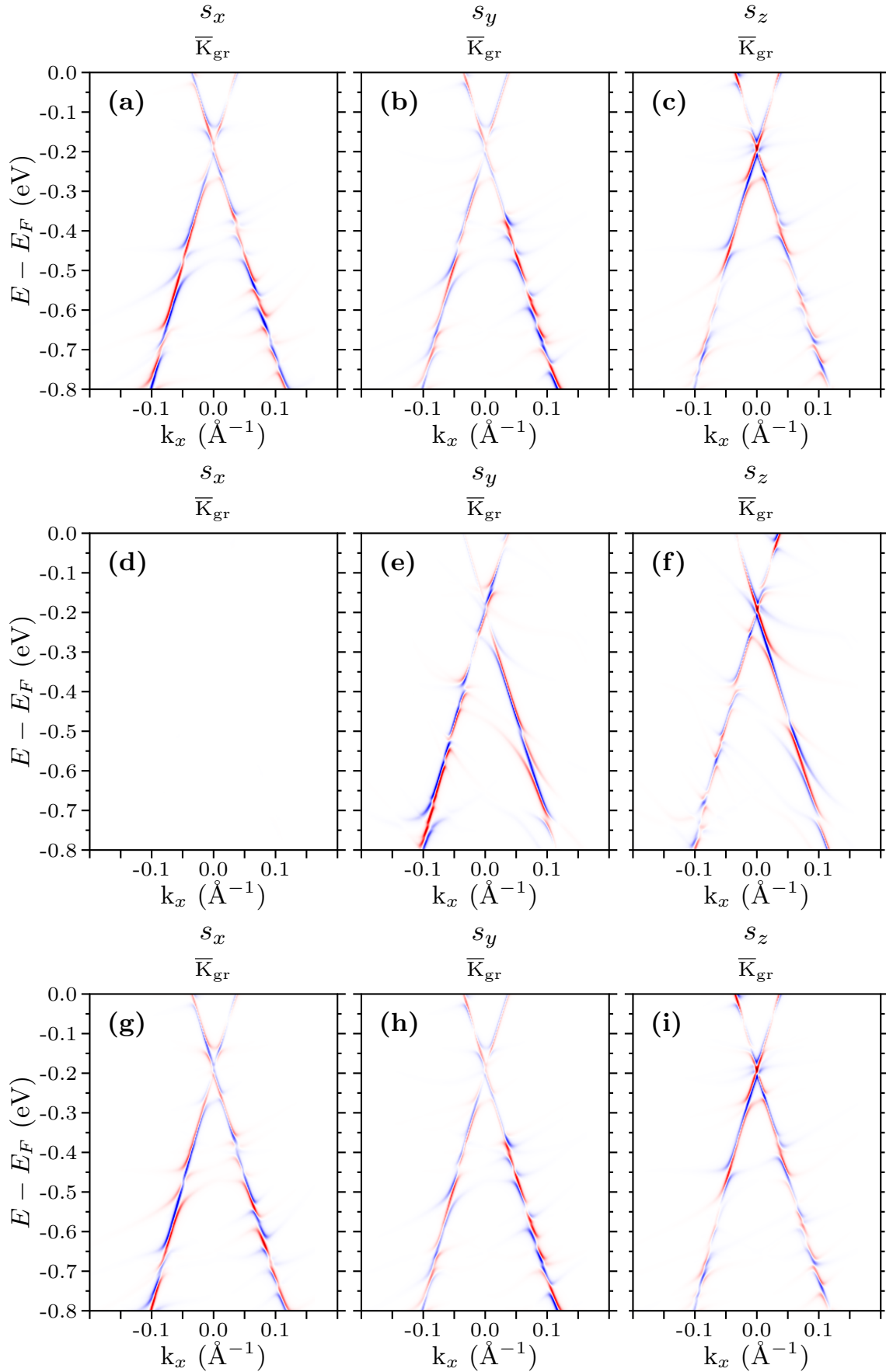
Figure 6. Graphene-projected wave vector and energy resolved spin density maps $s(k,E)$ for gr/Pb/Ir(111) after unfolding from the (8×8) supercell to the graphene (1×1) unit cell for the three rotational domains of Pb: domain1 (a,b,c), domain2 (d,e,f), domain3 (g,h,i). The corresponding supercells and the Brillouin zones are shown in Fig. 7.
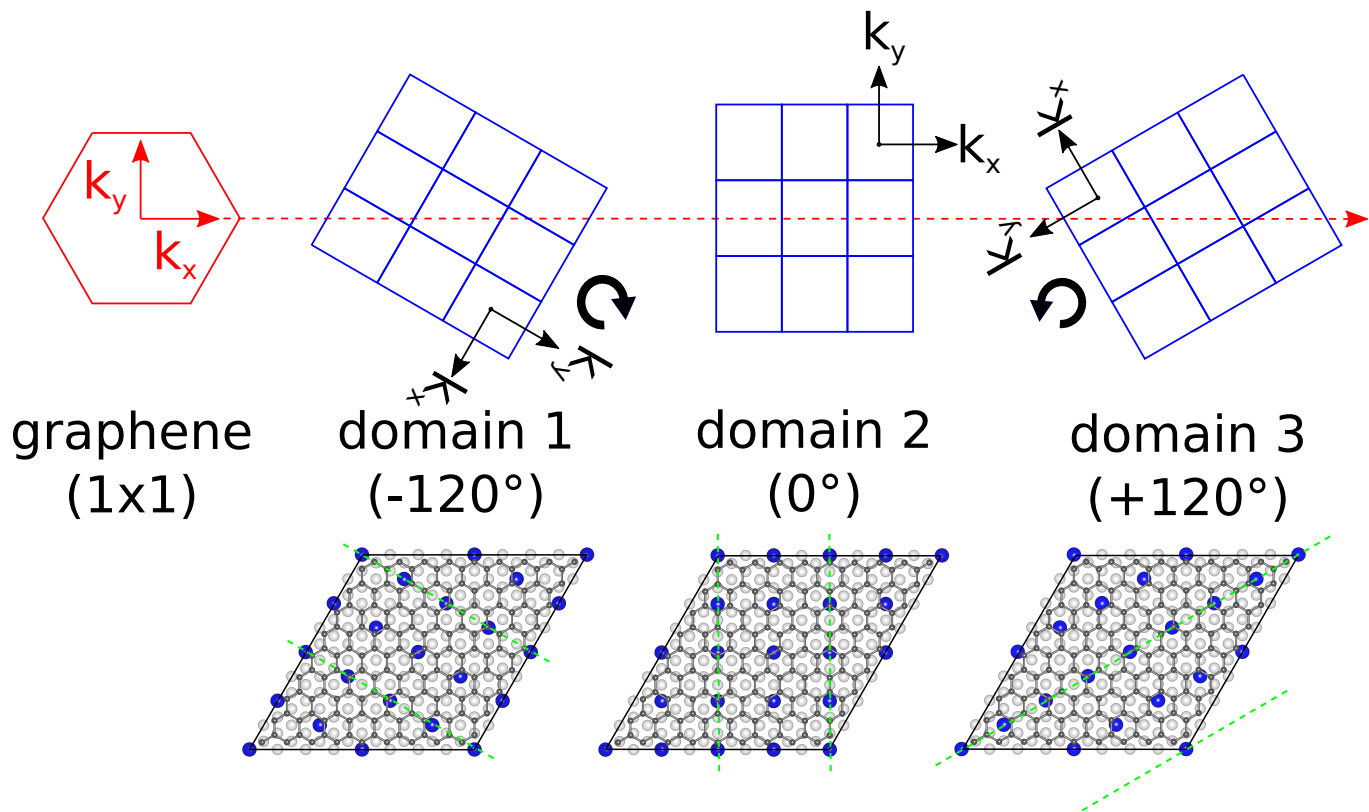
Figure 7. Top views of the gr/Pb/Ir(111) (8 × 8) supercells for the three rotational domains of Pb with the corresponding BZs. The red dashed line shows the direction of the band structure calculation, the result of which is shown in Fig. 6.
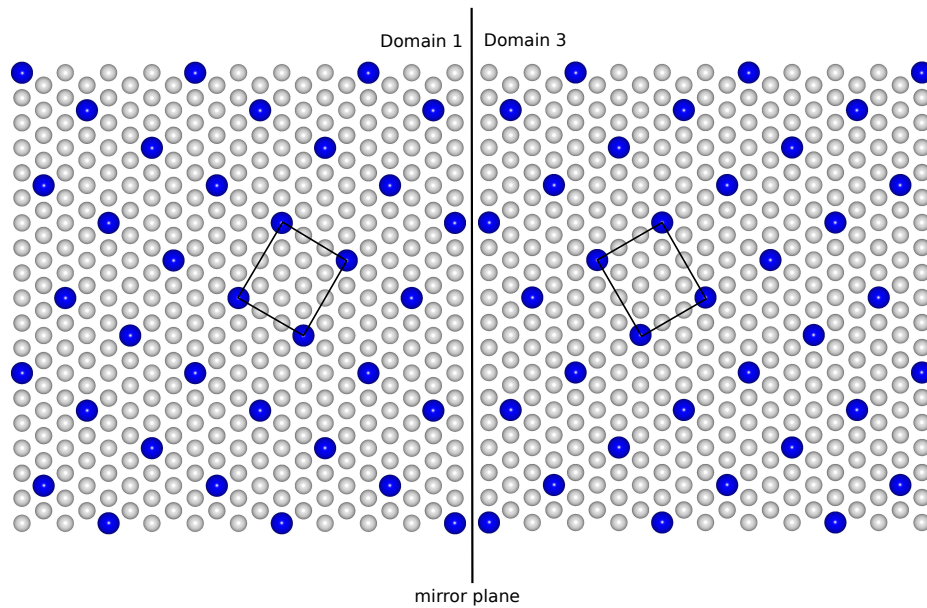

Figure 8. The top view of the Pb/Ir(111) domains 1 and 3 that are related by the mirror plane

VI.   CALCULATED SPIN-RESOLVED EDC

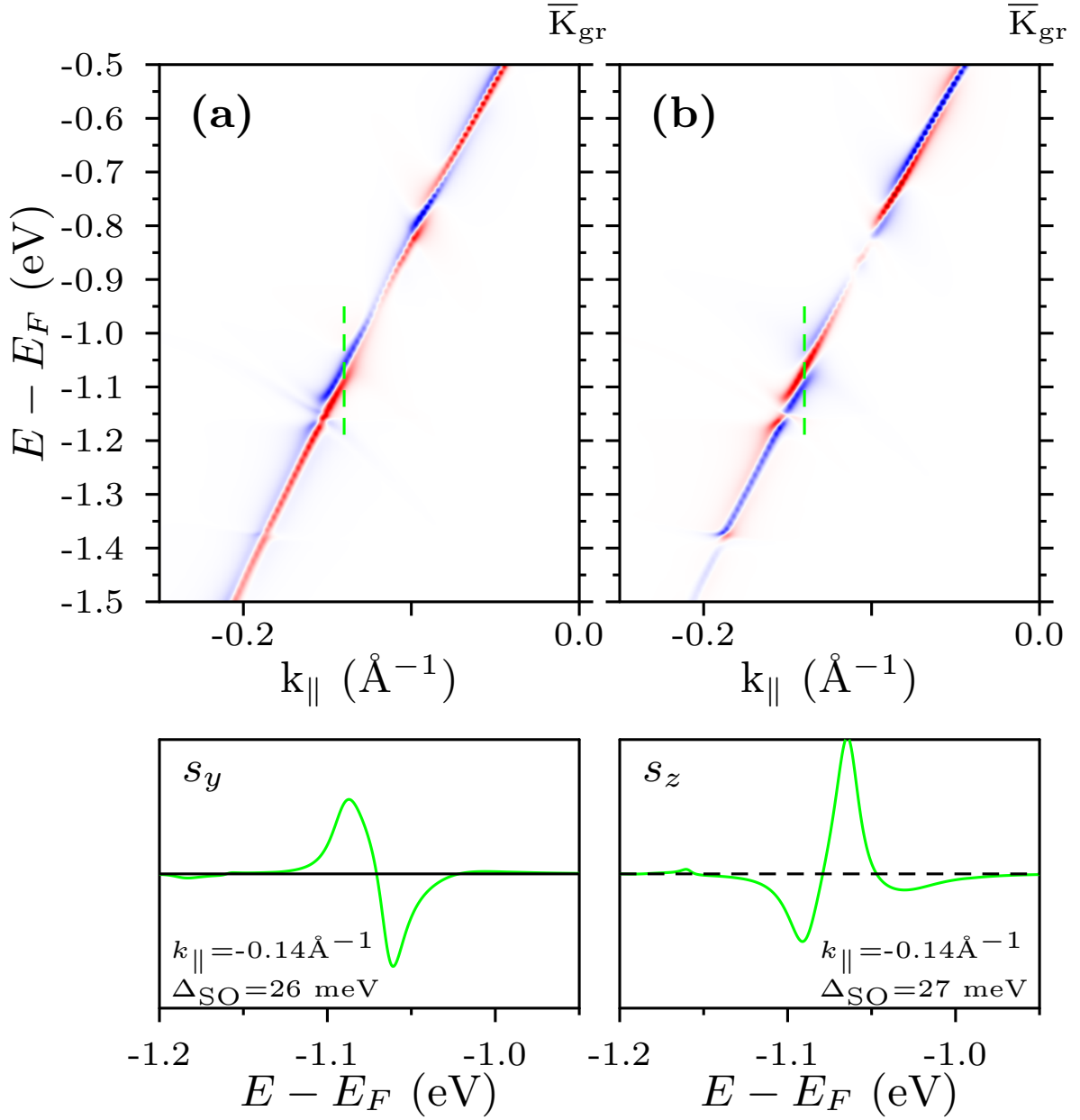
Figure 9. (a) Wave vector and energy resolved spin density $s(k, E)$ maps projected onto C atoms of the gr/Pb/Ir(111) semi-infinite surface system after unfolding from the (10×10) supercell to the graphene (1×1) unit cell: (a) and (b) show the in-plane and out-of-plane spin density maps. In the lower parts, the EDCs taken along the dashed green lines in (a) and (b) are shown.
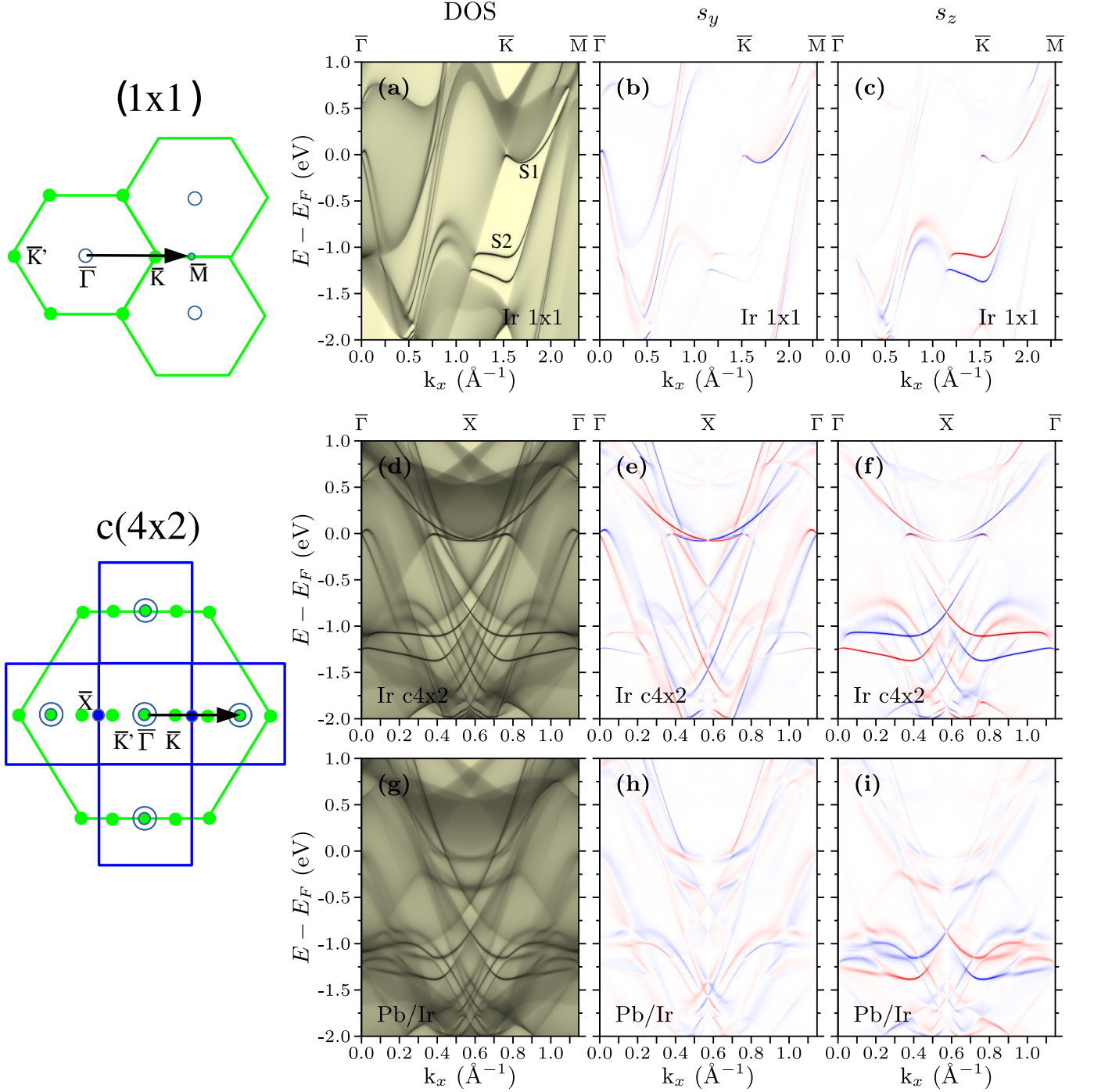
VII. BRILLOUIN ZONE FOLDING

Figure 10. Illustration of the Brillouin zone and band folding when changing the unit cell from (1×1) to $c(4 \times 2)$. (a) spin-averaged $PDOS(k, E)$, (b) in-plane spin density $s_y(k, E)$ and (c) out-of-plane spin density $s_z(k, E)$ maps projected on the first Ir layers of an Ir(111)-(1×1) semi-infinite surface calculated along the $\overline{\Gamma} - \overline{K} - \overline{M}$ path, as sketched in the inset on the left. (c), (d) and (e) same as (a-c) calculated along the $\overline{\Gamma} - \overline{X} - \overline{\Gamma}$ k-path after back-folding the (1×1) bands into the Brillouin zone of a $c(4 \times 2)$ supercell –shown in the inset at the left as blue rectangles in an extended zone scheme. The sketch with the (1×1) BZ (light green) and the location of the back-folded $\overline{K}$ and $\overline{K}'$ points (large green dots) is also shown. (g), (h) and (i) same as (d-f) but for the Pb/Ir(111) system in the $c(4 \times 2)$ supercell.

In Fig. 10(a) a 1.7 eV gap at $\overline{K}$ is clearly visible. It is crossed by two spin-split surface states S1 and S2 which correlate nicely with those measured in the ARPES studies [2, 3]. Also notice that the occupied surface states near the $\overline{K}$ point (S1 and S2) already mentioned, as well as other surface resonances at other locations in the (1×1) Brillouin zone, show both in-plane (s_y) and out-of-plane (s_z) spin components. The s_x component is negligible along the entire path due to the $p3m$ symmetry of the system.

By comparing the panels (d-f) and (g-i) in Fig. 10 one can see that the formation of the Pb $c(4 \times 2)$ layer on Ir(111) results in the increase of the energy width of the Ir(111) surface states and resonances, as well as the appearance of some splittings, but there are no qualitative differences in the spin texture as compared to the pure Ir(111) $c(4 \times 2)$ surface. As a result of the folding introduced by the Pb layer, the large projected gap at the $\overline{K}$ point [panel (a)] is closed [panels (d and g)], so that Ir(111) back-folded bands, hybridized with the Pb states, are the main responsibles of the interactions with the π-bands. Watch out that in gr/Ir(111) the π^*-bands are located at +150 meV (DP location) and above, with respect to the Fermi level, i.e., on top of projected bulk Ir bands above the gap centered at the $\overline{K}$ point of (1x1) Ir(111) Brillouin zone. Therefore, these π^*-bands are hybridized with Ir(111) states. However, in the case of gr/Pb/Ir(11), in which graphene is n-doped (the DP at about -250 meV), both π^*-bands and π-bands are hybridized with Pb/Ir(111) folded bands, although to a lesser extent as compared to the case of π^*-bands of gr/Ir(111) because, in this case, hybridization between gr bands and Pb/Ir(111) folded bands corresponds to a higher order perturbation, similar to the elastic width mechanism for the lifetime of Cs and Na (2x2) overlayers on Cu(111) quantum well states [4].

VIII.   SPIN ORBIT PROXIMITY EFFECT INDUCED BY A PB LAYER ON GRAPHENE.

A.   The model

We analyze the coupling between a layer of Pb atoms and graphene, see[5]. We neglect interactions between Pb atoms. The orbitals within each atom are coupled by the spin-orbit interaction[6]. The atomic states are classified by the total angular momentum, $j = \ell \pm 1/2$, where ℓ is the angular momentum, and j_z is the projection along the direction normal to the layer. These states can be written as

$$|j = \ell + 1/2, j_z\rangle = \alpha_{\ell,\ell_z} |\ell, \ell_z = j_z + 1/2, \downarrow\rangle + \beta_{\ell,\ell_z}|\ell, \ell_z = j_z - 1/2, \uparrow\rangle$$
$$|j = \ell - 1/2, j_z\rangle = \beta_{\ell,\ell_z} |\ell, \ell_z = j_z + 1/2, \downarrow\rangle - \alpha_{\ell,\ell_z}|\ell, \ell_z = j_z - 1/2, \uparrow\rangle \tag{1}$$

where α_{ℓ,ℓ_z} and β_{ℓ,ℓ_z} are coefficients which are determined by the strength of the spin-orbit coupling and the crystal field splitting between the orbitals $|\ell, \ell_z = j_z + 1/2, \downarrow\rangle$ and $\ell, \ell_z = j_z - 1/2, \uparrow\rangle$. The crystal field splitting determines the atomic on site energies ϵ_{ℓ,ℓ_z}. When $j_z = \ell + 1/2$ we have $\alpha_{j,j_z} = 0$ and $\beta_{j,j_z} = 1$, and the second combination in eq.(1) does not exist.

The coupling between the Pb orbitals to the graphene p_z orbitals are described by a tight binding parameters which can be calculated using the Slater Koster parameters[7]. The hoppings conserve the spin.

In the following, we will present calculations mostly using only four Pb atomic orbitals of the type in eq.(1). As described below, this choice is sufficient for an complete enumeration of the spin orbit couplings induced in graphene, and for an estimation of their relative strength. The total angular momenta are $j = \ell \pm 1/2$, and the projected components along the z direction are $j_z = \pm\ell_z \pm 1/2$, with ℓ and ℓ_z fixed.

We consider separately the case where the Pb atom lies below the center of an hexagon of carbon atoms (hollow site) and the case where the Pb atom lies below a carbon atom (top). In order to include all terms allowed by symmetry[6, 8], we include Pb d orbitals, $\ell = 2$, and p orbitals, $\ell = 1$.

In the hollow case, we couple the Pb orbitals to the six carbon p_z orbitals in the hexagon which surrounds it. The parameters of the model are: i) the hopping between nearest neighbor carbon orbitals, t, ii) the hoppings between the carbon and the Pb orbitals, $t_\pm$, and, iii) the energies of the Pb orbitals with respect to the Dirac energy of graphene, $\epsilon_\pm$. The couplings and energies are, in turn, determined by the couplings and energies associated to the atomic orbitals with well defined angular momentum, $t_{\ell=1,2}$ and $\epsilon_{\ell=1,2}$.

In the top case, we include the coupling of the Pb orbitals to the carbon orbital on top of the atom, and also the coupling to the three nearest carbon orbitals, so that the number of hopping parameters between the Pb and the carbon orbitals is four, $t_\pm^{i=top,n.n.}$.

The couplings between the graphene states at the Dirac point and Pb can be treated by perturbation theory when $t_{Pb-C}^2/(\epsilon_{Pb}t) \ll 1$, where t_{Pb-C} is the order of magnitude of the carbon - Pb hoppings, and ϵ_{Pb} is the order of magnitude of the Pb orbitals energies with respect to the energy of the Dirac point.

B.   Perturbation theory.

Including spin, graphene has eight Bloch states at the Dirac point, labelled by valley, sublattice, and spin. As each of these degrees of freedom can have two values, we can define three sets of operators, the identity in each subsector, and the Pauli matrices: $\mathbb{I}_\tau, \tau_{i=x,y,z}$, which acts on the valley index, $\mathbb{I}_\sigma, \sigma_{i=x,y,z}$, which acts on the sublattice index, and $\mathbb{I}_s, s_{i=x,y,z}$, which acts on the spin index. The eight states at the Dirac energy define a 8×8 Hilbert space, and operators acting within it can be written as a product of the $4 \times 4 \times 4$ operators described here.

In second order perturbation theory, the effective spin orbit couplings induced in graphene arise from virtual hoppings of electrons or holes from the graphene lattice to a given atomic orbital and back. Each combination of atomic orbitals of the type in eq.(1) contributes separately. Hence, in order to enumerate the number of possible terms, we need to consider those combinations which give rise to different couplings.

In order to preserve time reversal invariance, the inclusion of an atomic orbital labeled as $|\ell, \ell_z, s\rangle$ requires the inclusion of the orbital $\ell, -\ell_z, -s\rangle$, as they are related by time reversal symmetry. Hence, the minimum number of Pb orbitals required is four, $|\ell, \ell_z, \downarrow\rangle, |\ell, \ell_z - 1, \uparrow\rangle, |\ell, -\ell_z, \uparrow\rangle$, and $|\ell, -\ell_z + 1, \downarrow\rangle$.

The hoppings between graphene orbitals and Pb orbitals conserve spin, but the combinations in eq.(1) do not have a well defined spin. As a result, virtual hoppings via these states can give rise to spin flip processes, where a hopping of an electron with a given spin orientation residing in graphene into the Pb state is followed by the hopping from Pb to graphene of an electron with the opposite spin orientation.
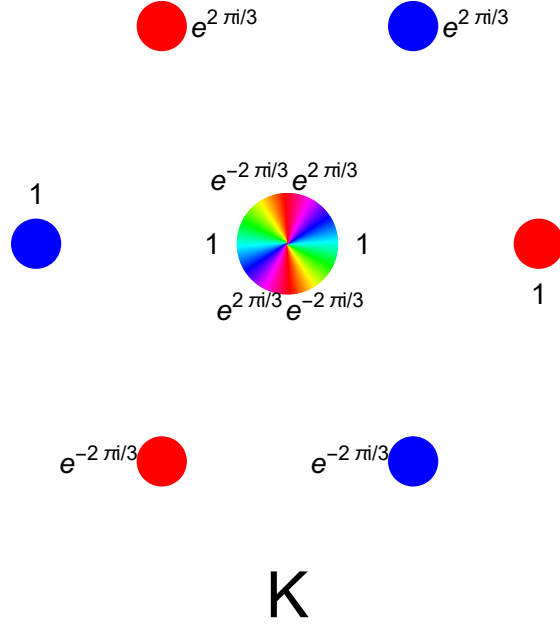
Figure 11. Sketch of the phases of the graphene wavefunctions at the K point (left), and at the K' point, right, and of the hoppings between the carbon and a Pb orbital with $\ell_z = 2$. The blue disks label the A sublattice, and the red disks the B sublattice.

1. Hollow position.

The Bloch states at the Dirac point are defined at different sites in the hexagon around the Pb atom, and they have different phases at each site. For instance, the state $|K, A, \uparrow\rangle$ has zero amplitude at the three B sites of the hexagon, and the phases at the three A sites are $\{1, e^{\pm(2\pi i)/3}\}$. The Slater-Koster combinations of parameters which describe the hoppings between an orbital with $\ell_z = j$ and the six orbitals around the hexagon also have phases, $t_i = t_\pm e^{(2\pi ijk)/6}$, where $k = 1, \cdots, 6$ labels the six carbon sites. A sketch of the phases is shown in Fig.[11].

The combination of the phases of the tight binding parameters and the phases of the Bloch states at the Dirac point leads to a number of interference effects. i) the effective hopping between any Bloch state and an atomic orbital with $\ell_z = 3n$, where n is an integer, vanishes, ii) atomic orbitals with $\ell_z = 3n + 1$ couple only to the $|A, K, \uparrow\downarrow\rangle$ and the $|B, K', \uparrow\downarrow\rangle$ states, and iii) atomic orbitals with $\ell_z = 3n + 2$, couple only to the $|B, K, \uparrow\downarrow\rangle$ and the $|A, K', \uparrow\downarrow\rangle$ states.

The hoppings from graphene into a Pb combination of the type in eq.(1) and back lead to spin conserving and spin flip processes. Taking into account the interference effects described above, the spin conserving processes lead to the effective hamiltonian

$$
\begin{aligned}
\mathcal{H}_1 &= -\frac{1}{2} \left[\frac{(\alpha_{\ell=2,\ell_z=1}t_{\ell=2})^2 + (\beta_{\ell=2,\ell_z=1}t_{\ell=1})^2}{\epsilon_{j=3/2}} + \frac{(\beta_{\ell=2,\ell_z=1}t_{\ell=2})^2 + (\alpha_{\ell=2,\ell_z=1}t_{\ell=1})^2}{\epsilon_{j=1/2}} \right] (\mathbb{I}_\tau \mathbb{I}_\sigma \mathbb{I}_s + \tau_z \sigma_z s_z) = \\
&= \Delta_{KM} \left(\mathbb{I}_\tau \mathbb{I}_\sigma \mathbb{I}_s + \tau_z \sigma_z s_z \right)
\end{aligned}
\tag{2}
$$

This term is the sum of a spin independent shift and an intrinsic spin-orbit coupling[9] of equal magnitude.

The spin flip term is

$$
\begin{aligned}
\mathcal{H}_2 &= - \left[\frac{2\alpha_{\ell=2,\ell_z=1}\beta_{\ell=2,\ell_z=1}t_{\ell=2}t_{\ell=1}}{\epsilon_{j=3/2}} + \frac{2\alpha_{\ell=2,\ell_z=1}\beta_{\ell=2,\ell_z=1}t_{\ell=2}t_{\ell=1}}{\epsilon_{j=1/2}} \right] (\tau_z \sigma_x s_y - \sigma_y s_x) = \\
&= \Delta_R \left(\tau_z \sigma_x s_y - \sigma_y s_x \right)
\end{aligned}
\tag{3}
$$

This is a Rashba term[9]. Comparing eq.(2) and eq.(3), we obtain $|\Delta_R| \leq |\Delta_{KM}|$.

The total hamiltonian is

$$
\mathcal{H} = \mathcal{H}_0 + \mathcal{H}_1 + \mathcal{H}_2
\tag{4}
$$

where $\mathcal{H}_0$ is the spin independent Dirac hamiltonian,

$$\mathcal{H}_0 = \mathbb{I}_s v_F \left(\tau_z \sigma_x k_x + \sigma_y k_y \right) \tag{5}$$

The dispersion around the Dirac energy is

$$\epsilon_{\vec{\mathbf{k}}} = \Delta_{KM} \pm \frac{\Delta_R}{2} \pm \sqrt{\left(\Delta_{KM} \pm \frac{\Delta_R}{2} \right)^2 + v_F^2 |\vec{\mathbf{k}}|^2} \tag{6}$$

The energies at the Dirac point are $\epsilon_D = \{0, 0, 2\Delta_{KM} \pm \Delta_R\}$.

2. Top sites.

We can follow the arguments in the preceding subsection, and analyze the case of a metal atom below a carbon atom. For the $c(4 \times 2)$ superlattice that we study, this implies that the metal atom is placed below a carbon atom in the A or in the B sublattice. The symmetry between the two honeycomb sublattices is broken.

There are no interactions between a metal orbital with $\ell_z \neq 0$ and the carbon p_z orbital above it. In order to be sufficiently general, we need to consider two cases, $\ell_z = 0$ and $\ell_z \neq 0$. The first case implies the existence of an atomic state of the form in eq.(1) which involves $|\ell, \ell_z = 0, \uparrow\rangle$ and $|\ell, \ell_z = 1, \downarrow\rangle$ and the state which can be obtained from the previous combination by time reversal symmetry.

We assume that the metal orbitals couple to the p_z orbitals in the atom directly above the metal atom, and to the three carbons at the nearest neighbor sites. Interference effects like those discussed in the previous subsection imply that the orbital with $\ell_z = 0$ metal orbital is decoupled from the projection of Dirac Bloch states at the nearest neighbor sites. This result, as well as the decoupling of $\ell_z \neq 0$ orbitals and the top carbon atom, imply that spin conserving effective interactions involve either the A or the B sublattice only, depending on whether the atomic state includes $\ell_z = 0$ orbitals or not. Summing contributions from the two types of metal states, we obtain for the spin conserving effective interactions

$$\mathcal{H}_1 = -\frac{1}{2} \left[\frac{(\alpha_{\ell=1,\ell_z=1} t_{\ell_z=1,n.n.})^2}{\epsilon_{j=3/2}} + \frac{(\beta_{\ell=1,\ell_z=1} t_{\ell_z=1,n.n.})^2}{\epsilon_{j=1/2}} \right] (\mathbb{I}_\sigma + \sigma_z)(\mathbb{I}_\tau \mathbb{I}_s + \tau_z s_z) -$$
$$- \left[\frac{(\beta_{\ell=1,\ell_z=1} t_{\ell_z=1,top})^2}{\epsilon_{j=3/2}} + \frac{(\alpha_{\ell=1,\ell_z=1} t_{\ell_z=1,top})^2}{\epsilon_{j=1/2}} \right] (\mathbb{I}_\sigma - \sigma_z)(\mathbb{I}_\tau \mathbb{I}_s) \tag{7}$$

These couplings break the symmetry between the two sublattices. We find, in addition, a spin flip term which involves also hopping between sublattices

$$\mathcal{H}_2 = -\left[\frac{\alpha_{\ell=1,\ell_z=1} \beta_{\ell=1,\ell_z=1} t_{\ell_z=1,n.n.} t_{\ell_z=1,top}}{\epsilon_{j=3/2}} + \frac{\alpha_{\ell=1,\ell_z=1} \beta_{\ell=1,\ell_z=1} t_{\ell_z=1,n.n.} t_{\ell_z=1,top}^2}{\epsilon_{j=1/2}} \right] (\tau_z \sigma_z s_y - \sigma_y s_x) \tag{8}$$

The total hamiltonian includes spin independent shifts, a Kane-Mele term, a Rashba term, and a term, $\propto \mathbb{I}_\sigma \tau_z s_z$, which breaks the symmetry between sublattices. This term has already been discussed already in relation to the effect of a WS$_2$ substrate on graphene[10].

The spin independent processes are proportional to $\propto t_{top}^2/\bar{\epsilon} - t_{n.n.}^2/\bar{\epsilon}$, where t_{top} and $t_{n.n.}$ are averages of the top and nearest neighbor hoppings, and $\bar{\epsilon}$ is an average of the orbital levels. The same type of orbitals give opposite signs for the Kane-Mele term at top and hollow positions[6]. Note, however, that the absolute magnitude of the term is not the same in both cases, as the interatomic distances, and the hoppings differ.

The spin flip processes are proportional to $\propto (t_{top} t_{bottom})/\bar{\epsilon}$. For $t_{top} \gg t_{n.n.}$ the spin independent interactions are much larger than the spin flip ones.

If we neglect the spin flip couplings, the four states at the Dirac point at a given valley are at energies $\epsilon_D \approx \{0, t_{n.n.}^2/\bar{\epsilon}, t_{n.n.}^2/\bar{\epsilon}, t_{top}^2/\bar{\epsilon}\}$.

C. Tight binding calculation.

We consider a metal atom in the hollow position. We describe the electronic structure of the atom using four orbitals, $|\ell = 2, \ell_z = 2, \downarrow\rangle, |\ell = 2, \ell_z = 1, \uparrow\rangle, |\ell = 2, \ell_z = 1, \uparrow\rangle$ and $|\ell = 2, \ell_z = 1, \downarrow\rangle$. The parameters (in eV) are
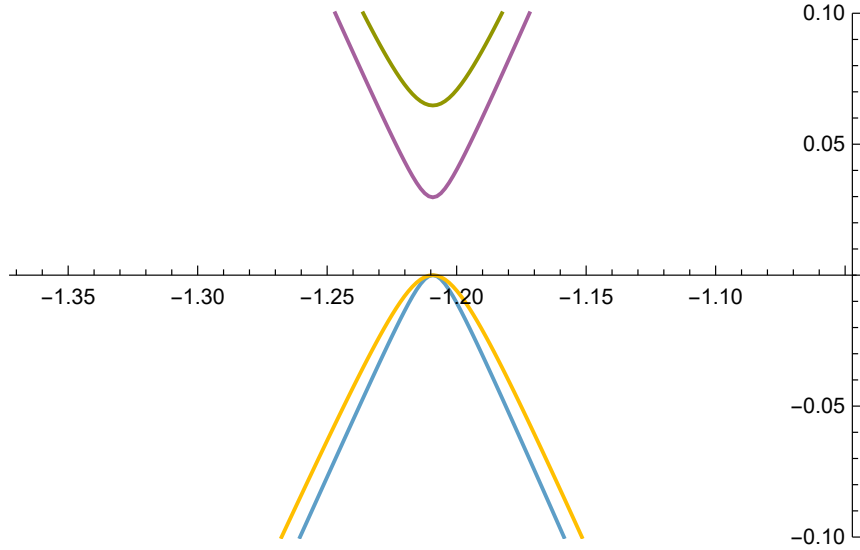
Figure 12. Bands of a $c(4 \times 2)$ graphene superlattice, with a metal atom in a hollow position. The parameters used are described in the text.
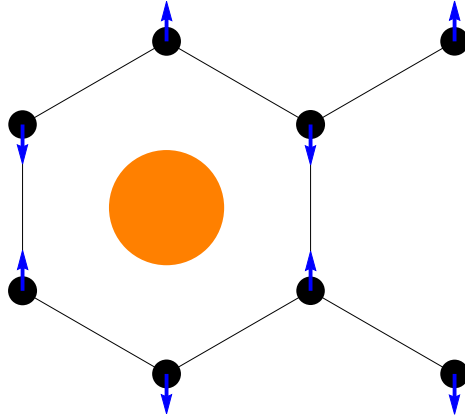

Figure 13. Out of plane spin components of the different eight C atoms in the $c(4 \times 2)$ graphene superlattice, s_z, for one of the states at $\epsilon_D = 0$ shown in Fig.[12]. Watch out the opposite spin components for C atoms belonging to different graphene sublattices.

$t = 3, t_{\ell=2} = 0.3, t_{\ell=1} = 0.1, \epsilon_{\ell=2} = -6, \epsilon_{\ell=1} = -4$ and the intratomic spin orbit coupling $\lambda = 3$. Results are shown in Fig.[12].

The results in Fig.[12] are consistent with the perturbative analysis described in (VIII B 1). At the Dirac point there are two degenerate states at $\epsilon_D = 0$, and two more states at higher energies. This result is confirmed by the charge and spin distribution for the states at the Dirac energy, see Fig.[13]. For the two states with $\epsilon_D = 0$ the in plane component of the spin vanishes. The states acquire an in plane component of the spin away from the Dirac point, as shown in Fig.[14].

An example of the bands with the metal in the top position is shown in Fig.[15]. The perpendicular spin distribution for a state with $\epsilon_D = 0$ is shown in Fig.[16]. The orbitals used have angular momentum $\ell = 1$. The orbital energies are $\epsilon_{\ell_z=1} = -6$ eV and $\epsilon_{\ell_z=0} = -4$ eV. The hopping parameters are $t_{\ell_z=0,top} = t_{\ell_z=1,top} = 0.5$ eV, and $t_{\ell_z=0,n.n.} = t_{\ell_z=1,n.n.} = 0.5$ eV. The results at the Dirac point are consistent with the perturbative analysis. The combination of a Kane-Mele term, $\propto \tau_z \sigma_z s_z$, and a valley dependent Zeeman coupling, $\propto \tau_z s_z$, makes the system gapless.
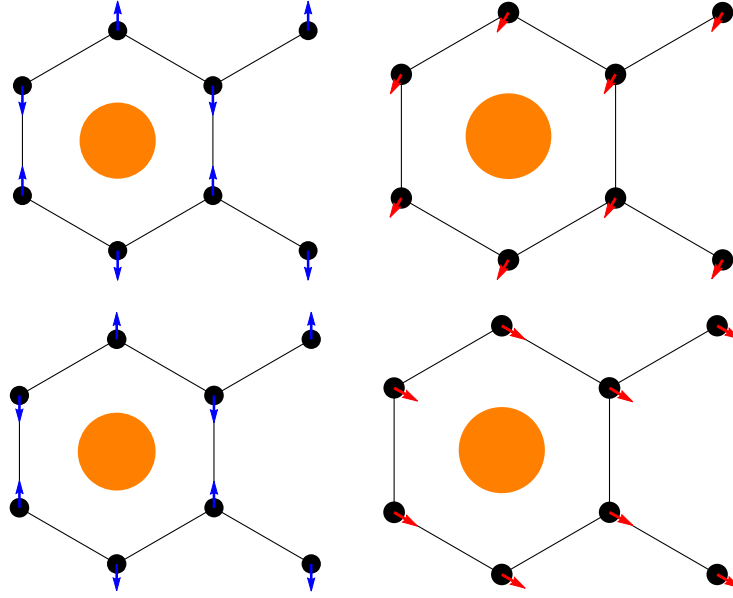
Figure 14. Left column: same as in Fig.[13] for states in the lowest band, displaced by $\Delta k_x = 0.01/a$ from the Dirac point, top, and by $\Delta k_y = 0.01/a$, bottom. Right column: results for the in plane magnetization and the same choice of parameters. The parameter a is the length of the unit cell of graphene. It is worth to mention that the cancellation of the out of plane spin components prevails for other states for the C-Pb registry, i. e., sublattice symmetry is preserved.
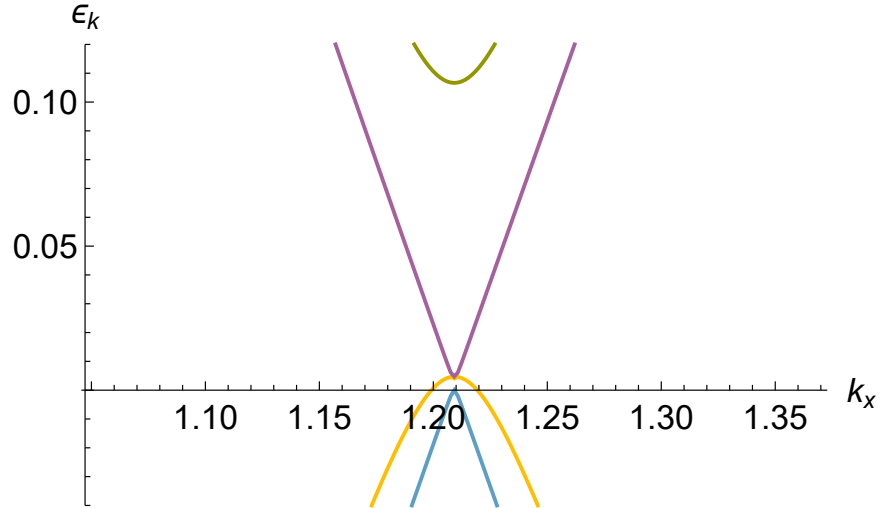

Figure 15. Bands of $c(4 \times 2)$ graphene superlattice, with a Pb atom in a top position. The parameters used are described in the text.

D. Discussion.

We have analyzed the induced spin-orbit coupling in graphene due to a superlattice of Pb atoms. We have studied the model by perturbative and numerical methods. The parameters used in the numerical tight binding model have the order of magnitude expected for the system. If we assume that the hopping between graphene and the metals decrease exponentially with the distance, typical values are in the range $\approx 0.1-0.5$ eV for distances of a few angstroms. The effective couplings are small, and we find that the numerical results agree well with perturbation theory.

The inclusion of $\ell = 1$ orbitals only leaves out spin orbit terms allowed by symmetry, like the Rashba term when the atom is in a hollow position[6, 8]. In order to avoid it, we have included d orbitals in the description of the metal
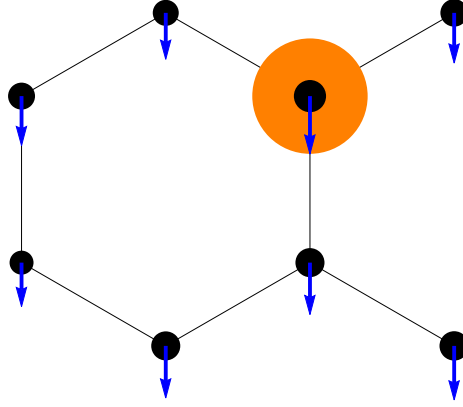
Figure 16. Out of plane spin component, s_z, in the superlattice cell for one of the states at $\epsilon_D = 0$ shown in Fig.[15]. Watch out that, in this case, the same spin components for C atoms belonging to different graphene sublattices appear giving rise to a net out-of-plane spin polarization as a consequence of the breakdown of sublattice symmetry.

atom. For atoms in the top position, we find a valley dependent Zeeman term[10], besides the Kane-Mele and Rashba couplings.

We have not considered the formation of bands in the metal layer. The distance between Pb atoms is larger than in bulk lead, and the electronic structure will be more localized. The hybridization between Pb orbitals at the momenta where the Dirac point of graphene is located, however, lowers the symmetry of the Pb Bloch orbitals hybridized with the graphene bands, and new terms can arise. We expect that the deviation of the Pb orbitals at the Dirac point from s, p or d symmetry to be small, as i) these symmetries are well defined at high symmetry points of the Brillouin Zone, and ii) the deviations arise from hybridizations between atomic orbitals with different symmetries at different points in the Pb lattice, which we expect to be small.

The results suggest that, both in the hollow and top positions, Pb orbitals induce mostly spin conserving (intrinsic) spin-orbit terms. The order of magnitude of these terms is $\propto 0.01 - 0.1$ eV. Pb atoms at hollow positions give rise to a gap at the Dirac point, while Pb atoms at top positions do not.
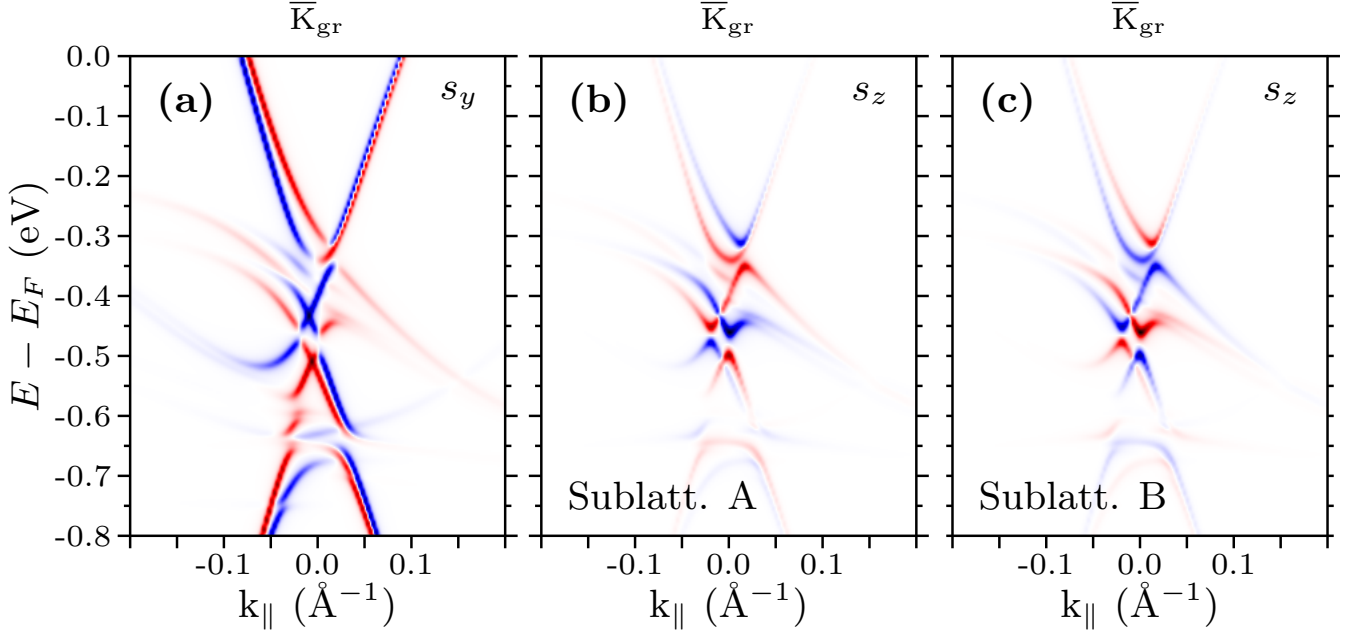
IX.   CANCELATION OF THE s_z COMPONENT IN GR/PB (10X10)

Figure 17. Graphene-projected wave vector and energy resolved spin density maps $s(k, E)$ for a gr/Pb bilayer after unfolding from the (10×10) supercell to the graphene (1×1) unit cell. Panel (a) shows the in-plane (s_y) spin component, while panels (b) and (c) show the A- and B-sublattice resolved out-of-plane component (s_z). It is seen that the A and B sublattices feature opposite s_z components which cancel one another upon integration over the two, as it should be due to the preservation of sublattice symmetry in the graphene/Pb (10×10) system.
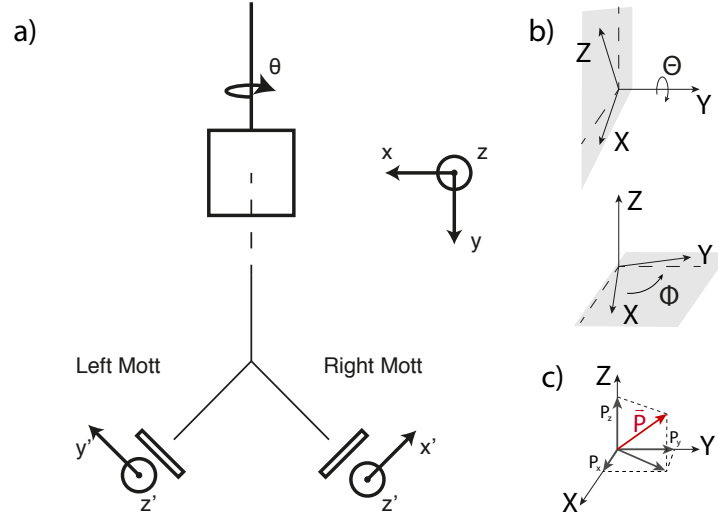
X. SARPES

Figure 18. (a) - experiment geometry [11, 12], (x, y, z) coordinates respect to sample and (x', y', z') to Mott detector channels. (b) - angles of rotation, Θ - around y axis and Φ around z. (c) - polarization vector and its P_x, P_y and P_z projections.

Spin resolved measurements of graphene/Ir(111) system intercalated with Pb atoms were performed at COPHEE beamline at SLS synchrotron. The geometry of the experiment is presented in fig.18. During measurements only the right (according the figure) detector was used. For the transformation of the spin polarization vector measured in the coordinate frame of the Mott detectors (spanned by the normals of the scattering planes of the four detector pairs) into the sample frame, the orientation of the manipulator needs to be incorporated. The conversion consists of three rotations about Euler angles: (i) azimuthal rotation about the analyzer lens axis by 45°, (ii) rotation by Θ ("polar" angle) about the primary axis of the manipulator, (iii) rotation by Φ (tilt angle) about the secondary axis of the manipulator. During the experiment, the angle Θ was 26° and the angle Φ was 0°. Thus, the polarization vector in the sample frame relates to the polarization in the Mott frame by an orthogonal matrix (a) [12]. If one sets ϕ to 0, as it was in our experiment, one gets the simplified transformation matrix (b).

$$(a) \begin{bmatrix} \frac{\cos\Theta}{\sqrt{2}} & -\frac{\cos\Theta}{\sqrt{2}} & -\sin\Theta \\ \frac{\cos\Phi-\sin\Theta\sin\Phi}{\sqrt{2}} & \frac{\cos\Phi+\sin\Theta\sin\Phi}{\sqrt{2}} & -\cos\Theta\sin\Phi \\ \frac{\sin\Phi+\sin\Theta\cos\Phi}{\sqrt{2}} & \frac{\sin\Phi-\sin\Theta\cos\Phi}{\sqrt{2}} & \cos\Theta\cos\Phi \end{bmatrix}$$

$$(b) \begin{bmatrix} \frac{\cos\Theta}{\sqrt{2}} & -\frac{\cos\Theta}{\sqrt{2}} & -\sin\Theta \\ \frac{1}{\sqrt{2}} & \frac{1}{\sqrt{2}} & 0 \\ \frac{\sin\Theta}{\sqrt{2}} & -\frac{\sin\Theta}{\sqrt{2}} & \cos\Theta \end{bmatrix}, if \ \phi = 0$$

Coordinates corresponding to the sample were denoted as (x, y, z) and those corresponding to the Mott detector were denoted as (x', y', z'). Thus transformation from experimental data (data from Mott detector channels) will have following form (we did transformation of polarization projection on corresponding axes):

$$\begin{pmatrix} P_x \\ P_y \\ P_z \end{pmatrix} = \begin{bmatrix} \frac{\cos\Theta}{\sqrt{2}} & -\frac{\cos\Theta}{\sqrt{2}} & -\sin\Theta \\ \frac{1}{\sqrt{2}} & \frac{1}{\sqrt{2}} & 0 \\ \frac{\sin\Theta}{\sqrt{2}} & -\frac{\sin\Theta}{\sqrt{2}} & \cos\Theta \end{bmatrix} \times \begin{pmatrix} P_{x'} \\ P_{y'} \\ P_{z'} \end{pmatrix}$$

In such geometry, the z axis corresponds to out-of-plane direction of spin polarization and y axis to in-plane direction. It was theoretically shown that for graphene/Pb/Ir system x component of spin polarization vector absents. Therefore from the upper equation one can obtain the spin polarization components y and z:

$$P_y = \sqrt{2}P_{x'} - \tan\Theta P_{z'}$$

$$P_z = \frac{P_{z'}}{\cos\Theta}$$

This polarization components are shown in Fig.3 of the paper at the bottom panels. In the middle panels of Fig.3 the total spin polarization P_t, calculated as modulus of spin polarization $\sqrt{P_x^2 + P_y^2 + P_z^2}$ multiplied by sign of P_y is presented. P_x is assumed to be equal 0. The upper panels in Fig.3 show the spin-resolved spectra ($I^\uparrow$ and $I^\downarrow$) calclulated as[11]:

$$I^\uparrow = \frac{1}{2}\left(I_{total}\right)\left(1 + P_t\right)$$

$$I^\downarrow = \frac{1}{2}\left(I_{total}\right)\left(1 - P_t\right)$$

For the used set-up, this transformation matrix is verified in other experiments [13, 14].

Fig. 19 displays the raw data in the detector coordinate frame. The raw data show a clear up-down signal in the spin asymmetry.
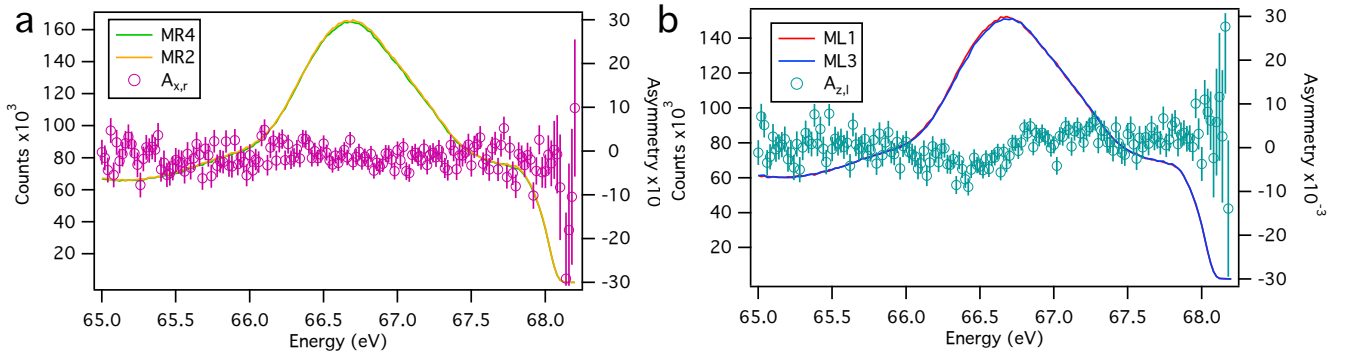

Figure 19. Raw spin-resolved ARPES spectra for graphene/Pb/Ir and the corresponding asymmetries in the spin detector coordinate frame for the x'-axis (a) and z'-axis (b) projections. The spectra were taken at k_x=0.1 Å^{-1} ($\overline{K}_{gr}$=0 Å^{-1}) along the $\overline{\Gamma K}$ direction.

[1] J. Warmuth, A. Bruix, M. Michiardi, T. Hänke, M. Bianchi, J. Wiebe, R. Wiesendanger, B. Hammer, P. Hofmann, and A. A. Khajetoorians, Phys. Rev. B **93**, 165437 (2016).
[2] I. Pletikosić, M. Kralj, P. Pervan, R. Brako, J. Coraux, A. T. N'Diaye, C. Busse, and T. Michely, Phys. Rev. Lett. **102**, 056808 (2009).
[3] I. Pletikosić, M. Kralj, D. Šokčević, R. Brako, P. Lazić, and P. Pervan, Journal of Physics: Condensed Matter **22**, 135006 (2010).
[4] C. Corriol, V. M. Silkin, D. Sánchez-Portal, A. Arnau, E. V. Chulkov, P. M. Echenique, T. von Hofe, J. Kliewer, J. Kröger, and R. Berndt, Phys. Rev. Lett. **95**, 176802 (2005).
[5] F. Calleja, H. Ochoa, M. Garnica, S. Barja, J. J. Navarro, A. Black, M. M. Otrokov, E. V. Chulkov, A. Arnau, A. L. Vázquez de Parga, F. Guinea, and R. Miranda, Nature Phys. **11**, 43 (2015).
[6] L. Brey, Phys. Rev. B **92**, 235444 (2015).
[7] J. C. Slater and G. F. Koster, Phys. Rev. **94**, 1498 (1954).
[8] C. Weeks, J. Hu, J. Alicea, M. Franz, and R. Wu, Phys. Rev. X **1**, 021001 (2011).
[9] C. L. Kane and E. J. Mele, Phys. Rev. Lett. **95**, 226801 (2005).
[10] Z. Wang, D. Ki, H. Chen, H. Berger, A. H. MacDonald, and A. F. Morpurgo, Nature Comm. **6**, 6339 (2015).
[11] F. Meier, J. H. Dil, and J. Osterwalder, New Journal of Physics **11**, 125008 (2009).
[12] G. Landolt, *Spin- and Angle-Resolved Photoelectron Spectroscopy on Topological Insulators and Bulk Rashba Systems*, Ph.D. thesis, University of Zurich (2014).

[13] B. Q. Lv, S. Muff, T. Qian, Z. D. Song, S. M. Nie, N. Xu, P. Richard, C. E. Matt, N. C. Plumb, L. X. Zhao, G. F. Chen, Z. Fang, X. Dai, J. H. Dil, J. Mesot, M. Shi, H. M. Weng, and H. Ding, Phys. Rev. Lett. **115**, 217601 (2015).
[14] J. Krempaský, H. Volfová, S. Muff, N. Pilet, G. Landolt, M. Radović, M. Shi, D. Kriegner, V. Holý, J. Braun, H. Ebert, F. Bisti, V. A. Rogalev, V. N. Strocov, G. Springholz, J. Minár, and J. H. Dil, Phys. Rev. B **94**, 205111 (2016).